Load-Independent Push–Pull Class E^2 Topology With Coupled Inductors for MHz-WPT Applications

Xiaosheng Huang, *Member, IEEE*, Zhikun Yu, Yi Dou, *Member, IEEE*, Shuyi Lin, Ziwei Ouyang, *Senior Member, IEEE*, and Michael A. E. Andersen, *Member, IEEE*

***Abstract*—This article investigates the modeling and implementation of the load-independent operation for the push–pull Class E topology with coupled inductors. The analytical modeling is first presented and provides a new design methodology, which distantly improves the soft-switching performance, load regulation, and efficiency compared with the conventional inductor-coupled Class E topology. An *LCC-S* resonant Class E^2 converter, which combines the load-independent inductor-coupled inverter and active rectifier, is proposed for MHz-wireless power transfer (MHz-WPT) applications. The active inductor-coupled Class E rectifier maintains soft switching, constant voltage gain, and zero-phase-angle input at various loads. A three-winding magnetic structure is also proposed to improve the coupled inductors by enhanced self-inductance, which features more effective harmonic suppression with lower magnetic losses and volumes. By the proposed methodology and the improved magnetic structure, the converter features negligible harmonic contents and maintains soft switching with a constant voltage conversion ratio over the entire load range. A 6.78-MHz WPT prototype was built to verify the proposed methodology with detailed parameter design and hardware implementation. The prototype realizes load-independent zero-voltage switching and maintains an approximately constant voltage gain with +5/−4% variance from no-load to 320-W output power. The measured dc–dc efficiency reaches 89.3% at 210 W.**

***Index Terms*—Active rectifier, Class E, coupled inductor, load-independent, wireless power transfer (WPT).**

I. Introduction

WIRELESS power transfer (WPT) based on the magnetic coupling is increasingly used in various applications, including portable devices, medical implants, unmanned aerial vehicles (UAV), and electric vehicles [1]–[5]. With the development of wide-bandgap (WBG) devices, MHz-WPT operating in industrial, scientific, and medical (ISM) band is becoming promising to improve system efficiency with volumetric and gravimetric power density, compared with most existing WPT systems operating at several hundred kHz.

In MHz-WPT systems, the inverters and rectifiers are to generate and rectify the high-frequency power transferred by the contactless magnetic resonant tanks. As the operating frequency increases to the multi-MHz range, soft-switching topologies and high-quality-factor magnetic components are crucial for systems' efficiency and reliability. The active full-bridge and half-bridge topologies have been widely used in WPT systems. They require fewer magnetic components and are conducive to realize higher power density [6], [7]. However, since the switching period is substantially shortened in the multi-MHz range, it requires complex gate driver control to perform reliable zero-voltage switching (ZVS) for the active bridges applied with variable load.

To avoid the inherent issues of active bridges, the resonant Class E topology and its derivative forms are preferred topologies for MHz-WPT systems [8]–[12]. The conventional Class E inverters comprise a low-side switch that can easily operate in the multi-MHz range. Generally, the switch realizes both zero-voltage and zero-voltage-derivative turn-ON at the optimal load. However, the soft-switching operation is sensitive to load variation. Although feedback control is a potential solution to adjust the switching behavior at various loads, it requires a complex design for reliable operation [11], [12].

The soft switching performance can be improved by using finite dc-feed inductance in open-loop Class E topologies with variable load. Roslaniec *et al.* [13] implement an experiment-based approach to realize nearly invariant ZVS operation over a wide load range. Aldhaher *et al.* [14] introduce the load-independent single-switch Class E topology into MHz applications. In theory, the load-independent operation achieves prefect ZVS and constant voltage gain regardless of load variation. Nevertheless, the much lower dc-feed inductance results in dramatically increase of harmonic currents on dc sides. The harmonics will cause not only substantial losses but also electromagnetic interference (EMI) issues.

Interleaving approaches can be implemented to noticeably reduce the harmonic contents [15]–[21]. By using two switching units operating in push–pull mode, the fundamental and

Manuscript received November 4, 2021; revised December 28, 2021; accepted February 3, 2022. Date of publication February 10, 2022; date of current version March 24, 2022. This work was supported in part by the National Natural Science Foundation of China under Grant 51607039, in part by the Natural Science Foundation of Fujian Province of China under Grant 2019J01772, in part by the Science and Technology Planning Project of Fujian Province under Grant 2021H0024, and in part by the Science and Technology Planning Project of Fuzhou under Grant 2021-P-051. Recommended for publication by Associate Editor T. Mishima. *(Corresponding author: Xiaosheng Huang.)*

Xiaosheng Huang is with the School of Electronic, Electrical Engineering and Physics, Fujian University of Technology, Fuzhou 350118, China, and also with Postdoctoral Research Station, Changshu Switchgear Mfg. Company, Ltd., Changshu 215500, China (e-mail: hxs@fjut.edu.cn).

Zhikun Yu and Shuyi Lin are with the School of Electronic, Electrical Engineering and Physics, Fujian University of Technology, Fuzhou 350118, China (e-mail: yuzhikun1996@qq.com; linshuyi1985@qq.com).

Yi Dou, Ziwei Ouyang, and Michael A. E. Andersen are with the DTU Elektro, Technical University of Denmark, 2800 Kongens Lyngby, Denmark (e-mail: yi.dou@outlook.com; zo@elektro.dtu.dk; ma@elektro.dtu.dk).

Color versions of one or more figures in this article are available at https://doi.org/10.1109/TPEL.2022.3150175.

Digital Object Identifier 10.1109/TPEL.2022.3150175

odd-order harmonics circulate within the units, while only the even-order harmonics flow into dc sides. The design process is basically the same as single-switch inverters/rectifiers. Liu and Chen [18] use an enhanced push–pull Class E inverter to power multiple reconfigurable receivers of dual-band WPT systems. In [19], the active push–pull Class E rectifier achieves the load-independent operation and has zero-phase-angle (ZPA) input over the load range. Gu *et al.* [20] propose a push–pull Class Φ_2 inverter, which features very low input current ripple and the load-independent ZVS. And, the push–pull Φ_2 was implemented in a 1.7-KW 6.78-MHz WPT system [21].

It is noticed that the discrete magnetic components dominate the size of the power stage, while also limiting the further power density improvement of the system. Air-core or low-permeability-core inductors usually perform high-quality-factors in the MHz region, but it is challenging to implement compact inductors for Class E inverters/rectifiers [7], [22]–[26].

An investigation has been reported in [27] to integrate and couple the inductors of the push–pull Class E inverters. The coupled inductor was also implemented for active rectification [28]. This integration reduces magnetic component count and volumes. Moreover, the coupled inductors perform noticeable suppression of even-order harmonics on dc sides. Nevertheless, the existing design cannot achieve the load-independent soft-switching, which is even critical for MHz-WPT systems. The involved magnetic coupling breaks the previous circuit model achieving load-independent operation.

This article investigates the modeling, implementation, and improvement of the inductor-coupled push–pull Class E topology achieving load-independent operation, which realizes soft switching, low-harmonic contents, and constant voltage gain over the entire load range. Section II presents the deduction and obtains a unique parameter set that achieves the load-independent operation, which distantly improves the soft-switching performance and load regulation compared with the conventional inductor-coupled Class E topology in [27]. Section III discusses the active coupled-inductor Class E rectifier achieving ideal ZVS and ZPA input with variable load. An *LCC-S* resonant Class E^2 topology is thus proposed to achieve load-independent soft-switching and constant output voltage over the entire load range. Furthermore, an improved magnetic structure is proposed to implement the coupled inductors with enhanced self-inductance, which performs much better harmonic suppression with lower losses and volumes than the previous work. In Section IV, we built a 6.78-MHz WPT prototype to verify the proposed methodology with detailed parameter design and hardware implement. The experimental result is discussed and compared with our previous work in Section V. It shows expected soft-switching performance, low-harmonic contents, and efficiency improvement. Finally, Section VI concludes this article.

II. Modeling of Load-Independent Operation for Inductor-Coupled Push–Pull Class E Inverters

The load-independent single-switch Class E topology has been verified and implemented [14], [29]. Nevertheless, the involved magnetic coupling breaks the previous circuit model.

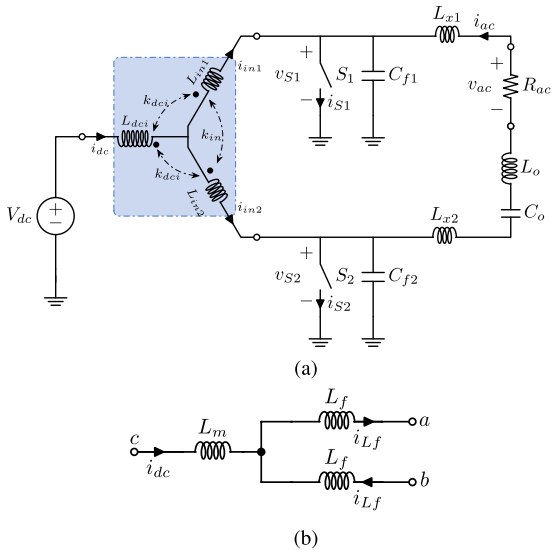

Fig. 1. (a) Push–pull Class E inverter with three-winding coupled inductor. (b) Equivalent decoupled circuit of coupled inductor. The output filter (L_o and C_o) resonates at the operation frequency. L_x is the additional inductance, which can be implemented by individual inductors or merges with L_o.

Thus, in this section, we derive the new circuit operating model for the inductor-coupled push–pull Class E topology.

A. Circuit Analysis

Fig. 1 illustrates the inductor-coupled push–pull Class E inverter. The proposed topology comprises a three-winding magnetic structure and additional inductance L_x, both of which have not been discussed in the previous work [27]. The additional inductance causes inherent differences in circuit operation since it changes the resonant network. To simplify the analysis, assumptions are made as follows.

1) The switches have zero ON-resistance and infinite OFF-resistance. The passive components are lossless.

2) S_1 is ON during $0 < \omega t \leq \pi$ and OFF during $\pi < \omega t \leq 2\pi$, where ω is the angular velocity. In contract, S_2 is OFF during $0 < \omega t \leq \pi$ and ON during $\pi < \omega t \leq 2\pi$. Since the switches operate at differential mode, the switch voltage can be defined as $v_S(\omega t) = v_{S1}(\omega t) = v_{S2}(\omega t + \pi)$.

3) The coupled inductor has large enough self-inductance, which makes the current ripples of $i_{\rm dc}$ negligible.

4) The characteristic impedance $\sqrt{L_o/C_o}$ of the output filter is high enough to form a sinusoidal output current $i_{\rm ac}$ with phase φ and amplitude $I_{\rm ac}$, i.e.,

$$i_{\rm ac}(\omega t) = I_{\rm ac} \cdot \sin(\omega t + \varphi). \tag{1}$$

As in Fig. 1(b), the three-winding coupled inductor can be decoupled to the mutual-inductance L_m and the leakage-inductance L_f, of which modeling is presented in Section III. This magnetic structure is proposed to enhance the equivalent self-inductance, which dominates the harmonic suppression. With proper winding arrangement, the inductance satisfies $L_m \gg L_f$, and thus the current ripples of $i_{\rm dc}$ are eliminated. Hence, the winding currents can be defined as $i_{Lf}(\omega t) = i_{in1}(\omega t) = i_{in2}(\omega t + \pi)$. Then, i_{Lf} during $\pi < \omega t \leq 2\pi$ can be

expressed by

$$i_{Lf}(\omega t) = I_{L_f\pi} - \frac{1}{\omega L_e}\int_{\pi}^{\omega t} v_S(\omega t_1)d\omega t_1 \tag{2}$$

where $L_e = 2L_f$, and $I_{L_f\pi}$ is the initial value of I_{Lf} at $\omega t = \pi$. Thus, the OFF-state switch voltage for $\pi < \omega t \leq 2\pi$ satisfies

$$\omega C_f \cdot \frac{dv_S(\omega t)}{d\omega t} = i_{Lf}(\omega t) + i_{\text{ac}}(\omega t). \tag{3}$$

Differentiating both sides gives

$$\frac{1}{q_e^2}\frac{d^2 v_{Sn}(\omega t)}{d\omega t^2} + v_{Sn}(\omega t) - p_e \cdot \cos(\omega t + \varphi) = 0 \tag{4}$$

of which the general solution is given by

$$v_{Sn}(\omega t) = \xi_1 \cos(q_e \omega t) + \xi_2 \sin(q_e \omega t) - \xi_e q_e \cos(\omega t + \varphi) \tag{5}$$

where ξ_1 and ξ_2 are the coefficients related to the circuit parameters of the inverter. v_{Sn} is the switch voltage normalized by V_{dc}, and

$$\xi_e = \frac{q_e p_e}{1 - q_e^2} \tag{6}$$

$$q_e = \frac{1}{\omega\sqrt{L_e C_f}} \tag{7}$$

$$p_e = \frac{I_{\text{ac}} \cdot \omega L_e}{V_{\text{dc}}} \tag{8}$$

where p_e is defined as the load factor representing the output current limited by the load resistance. To find the expressions of ξ_1, ξ_2, the initial conditions at $\omega t = \pi$ can be used as follows.

The inherent zero-voltage turning-OFF condition of S_1 is expressed as

$$v_{Sn}(\pi) = 0 \tag{9}$$

and the voltage-second balance of L_f is given by

$$\int_{\pi}^{2\pi} v_{Sn}(\omega t_1)d\omega t_1 = 2\pi. \tag{10}$$

Thus, the expressions of ξ_1 and ξ_2 are solved according to the two initial conditions, i.e.,

$$\begin{aligned}\xi_1 = \frac{-q_e\xi_e}{1-\cos(\pi q_e)}\,&[(2q_e\sin(\varphi) + 2\pi/\xi_e)\sin(\pi q_e)\\ &+ \cos(\varphi)\cos(\pi q_e)\,(1 - 2\cos(\pi q_e)) + \cos(\varphi)]\\ \xi_2 = \frac{q_e\xi_e}{1-\cos(\pi q_e)}\,&[(2q_e\sin(\varphi) + 2\pi/\xi_e)\cos(\pi q_e)\\ &- \cos(\varphi)\sin(\pi q_e)\,(1 - 2\cos(\pi q_e))]\,.\end{aligned} \tag{11}$$

Hence, the normalized switch voltage v_{Sn} is expressed as a function of three variables (q_e, p_e, and φ), which are crucial for modeling the following criteria achieving load-independent operation. It is worth noting that (11) has fewer variables than that in [27], where the sets of four variables are calculated numerically.

The following section obtains a unique and unreported analytical parameter set of the proposed topology achieving load-independent soft-switching and constant voltage gain.

B. Criteria of Load-Independent Operation

Since v_{Sn} acts a voltage source for the output. To analyze the output voltage with load variation, v_{Sn} can be separated into the active part (V_{Rn}) and the reactive part (V_{Xn}) by Fourier series as

$$V_{Rn} = \frac{1}{\pi}\int_{\pi}^{2\pi} v_{Sn}(\omega t)\sin(\omega t + \varphi)d\omega t \tag{12}$$

$$V_{Xn} = \frac{1}{\pi}\int_{\pi}^{2\pi} v_{Sn}(\omega t)\cos(\omega t + \varphi)d\omega t. \tag{13}$$

Deriving (12) and (13) with respect to the load factor p_e gives

$$\frac{dV_{Rn}}{dp_e} = \frac{q_e^4(\cos(2\varphi) - 1)(\cos(\pi q_e) + 1)}{\pi(q_e^2 - 1)^2(\cos(\pi q_e) - 1)} \tag{14}$$

$$\begin{aligned}\frac{dV_{Xn}}{dp_e} = &\frac{2q_e^4\cos(\varphi)(\cos(\pi q_e) + 1)}{\pi(q_e^2 - 1)^2(1 - \cos(\pi q_e))}\cdot\sin(\varphi)\\ &+ \left[\frac{2q_e\sin(\pi q_e)}{\pi(q_e^2 - 1)(1 - \cos(\pi q_e))} + \frac{1}{2}\right]\cdot\frac{q_e^2}{q_e^2 - 1}.\end{aligned} \tag{15}$$

Let $\varphi = \pi$ or 0 results

$$\left.\frac{dV_{Rn}}{dp_e}\right|_{\varphi=\pi,0} = 0. \tag{16}$$

The two particular values of φ lead to a same result. Therefore, V_{Rn} is irrelevant to load variation when $\varphi = \pi$. Then, (15) can be simplified as

$$\begin{aligned}\xi_4 = &\left.\frac{dV_{Xn}}{dp_e}\right|_{\varphi=\pi}\\ = &\left[\frac{2q_e\sin(\pi q_e)}{\pi(q_e^2 - 1)(1 - \cos(\pi q_e))} + \frac{1}{2}\right]\cdot\frac{q_e^2}{q_e^2 - 1}.\end{aligned} \tag{17}$$

As q_e depends on circuit parameters, V_{Xn} is proportional to p_e defined in (8). The voltage gain G_v can be expressed as

$$G_v = \frac{V_{\text{ac}}}{V_{\text{dc}}} = 2\cdot\left|j\cdot p_e\left(\xi_4 + \frac{L_x}{L_e}\right) + V_{R_n}\right| \tag{18}$$

where V_{ac} is the amplitude of v_{ac}. Thus, the reactive part of V_{Sn} can be compensated by fixed inductance given by

$$L_x = -\xi_4 L_e \tag{19}$$

Therefore, the compensated voltage-gain is given by

$$G_v = \frac{4q_e\sin(\pi q_e)}{(\cos(\pi q_e) - 1)(q_e^2 - 1)} \tag{20}$$

which is load-independent. The value of q_e achieving ZVS turn-ON can be obtained by solving v_{Sn} at $\omega t = 2\pi$, i.e.,

$$v_{Sn}(2\pi) = \frac{2\pi q_e\sin(\pi q_e)}{(1 - \cos(\pi q_e))} = 0 \tag{21}$$

which gives

$$q_e = 1. \tag{22}$$

Since the denominator of (15) cannot be zero, the limit method can be applied to evaluate the compensation coefficient, and

gives

$$\xi_4 = -\frac{1}{8} \tag{23}$$

which results in a compensated voltage gain irrelevant to load variation, i.e.,

$$G_v = \pi. \tag{24}$$

Meanwhile, the v_{Sn} can be simplified as

$$v_{Sn}(\omega t) = \sin(\omega t)\left[p_e\left(\frac{3\pi}{4} - \frac{\omega t}{2}\right) - \pi\right] \tag{25}$$

thus, the switch voltage has no high-order harmonics at no-load condition ($p_e = 0$).

As a result, (22) and (23) form a unique parameter set, which achieves load-independent ZVS turn-ON and maintains a constant voltage gain of π irrelevant to load resistance.

C. Theoretical Parameters and Waveforms

Based on applicable specifications, the rated condition can be designed where the switches achieve both ZVS and zero-current-switching (ZCS) turn-ON. Thus, the inverters perform soft switching over the entire load range and prevent reverse conducting at the switches' OFF-state.

The value of load factor p_e achieving ZCS turn-ON can be obtained by solving

$$\left.\frac{dv_{Sn}}{d\omega t}\right|_{\omega t = 2\pi} = -\frac{\pi}{4} \cdot p_e - \pi = 0 \tag{26}$$

which gives

$$p_{e\_r} = -4. \tag{27}$$

This ZCS condition is involved to form an equation set for calculating the practical circuit parameters as

$$R_{\text{ac\_}r} = \frac{V_{\text{dc}}^2 G_v^2}{2P_{\text{out\_}r}} \tag{28}$$

$$R_{\text{dc\_}r} = \frac{V_{\text{dc}}^2}{P_{\text{out\_}r}} \tag{29}$$

$$L_f = \frac{R_{\text{dc\_}r} G_v}{\omega} \tag{30}$$

$$L_x = 0.25 L_f \tag{31}$$

$$C_f = \frac{1}{2L_f \cdot \omega^2} \tag{32}$$

where $P_{\text{out\_}r}$ is the inverter's rated output power. $R_{\text{dc\_}r}$ and $R_{\text{ac\_}r}$ are the rated input and load resistance, respectively. It can be seen that the circuit parameters have constant coefficients. Equations (28)–(32) provide a concise guideline to design practical systems.

The switch voltage at various loads can be calculated according to (25), where R_{ac} is inversely proportional to p_e due to the constant voltage gain. As in Fig. 2(a), the switch maintains ZVS as load varies. Meanwhile, it will conduct reversely during a particular interval when R_{ac} is greater than the rated value. For the MOSFET or GaN FET-based systems, the semiconductor devices have a limited reverse conduction voltage drop, which will cause additional losses and affect the voltage gain. Therefore, the inverter can prevent reverse conducting of the switches at OFF-state over the designed load range (i.e., R_{ac} varies from the rated value to infinity). The peak voltage increases as R_{ac} decreases. The maximum v_{Sn} reaches 4.575 at $0.5 \cdot R_{\text{ac\_}r}$, and 3.639 at $R_{\text{ac\_}r}$. The reverse voltage usually causes unexpected conducting of practical semiconductor devices and affect the load-independent operation.

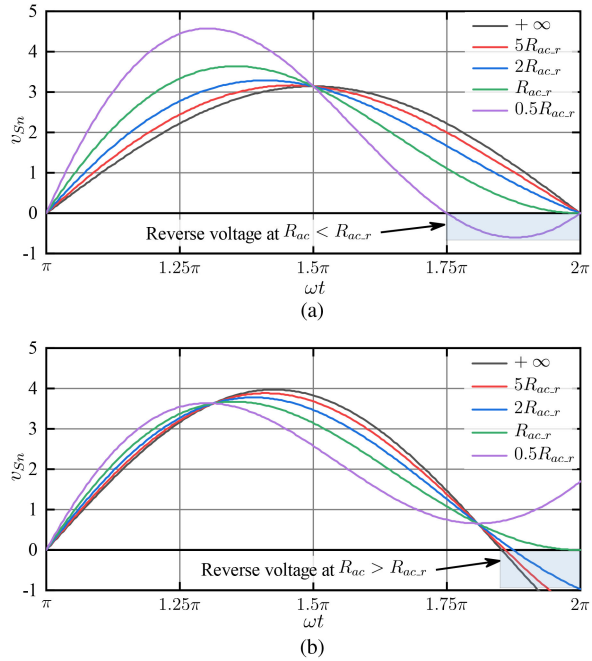

Fig. 2. Normalized switch voltage v_{Sn} versus load resistance R_{ac}. The two models perform noticeably different switching features. (a) Proposed model achieving load-independent ZVS (this article). The switches of proposed model achieve ideal ZVS turn-ON over the designed load range. (b) Conventional model in [27]. The switch in conventional model realizes ZVS turn-ON at the rated load but becomes non-ZVS at light loads.

The switching behavior is quite different from that in [27]. As shown in Fig. 2(b) where the conventional model achieves ZVZCS turn-ON at rated load, but turns to non-ZVS at $R_{\text{ac}} > R_{\text{ac\_}r}$. Using lower q_e can reduce switch voltage offsets of the conventional model and achieve better ZVS behavior. Nevertheless, the coupled inductor's current amplitude will substantially increase and cause unbearable losses.

In contrast, the proposed model achieves strict ZVS turn-ON over the entire load range without compromising the winding currents. Thus, the soft-switching performance is distinctly improved than before. The normalized i_{Lf} is given by

$$i_{Lfn}(\omega t) = \frac{i_{Lf}(\omega t)}{I_{dc\_r}} = \frac{2}{p_{e\_r} \cdot G_v} \cdot \begin{cases} \int_\pi^{\omega t} v_{Sn}(\omega t_1 + \pi) d\omega t_1 - \frac{\pi p_e}{4} + 1 & 0 < \omega t \le \pi \\ -\int_\pi^{\omega t} v_{Sn}(\omega t_1)) d\omega t_1 - \frac{\pi p_e}{4} + 1 & \pi < \omega t \le 2\pi. \end{cases} \tag{33}$$

As illustrated in Fig. 3, the winding currents of L_{in} maintain an amplitude of $0.5 \cdot I_{\text{dc\_}r}$ at various loads, and it is sinusoidal at no-load condition. As the amplitude keeps relatively large over

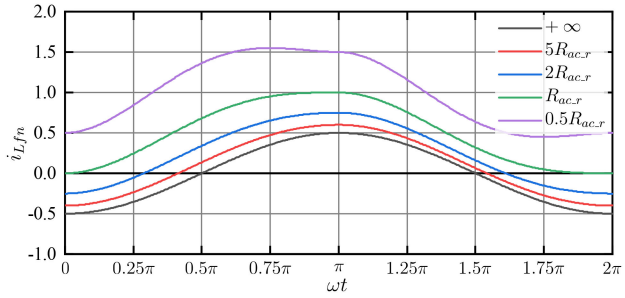

Fig. 3. Normalized winding current i_{Lfn} versus load resistance R_{ac}. The amplitude of i_{Lfn} is nearly constant as R_{ac} varies.

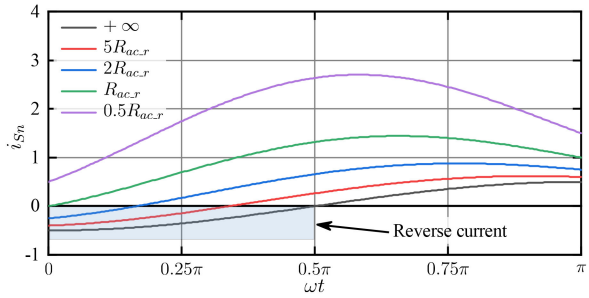

Fig. 4. Normalized switch current i_{Sn} versus load resistance R_{ac}. The amplitude increases as R_{ac} decreases, and the switches conduct reversely at the beginning of each ON-state period when $R_{\text{ac}} > R_{\text{ac\_}r}$.

the entire load range, the coupled inductor occupies a substantial part in the total loss.

As illustrated in Fig. 4, the switch achieves both ZVS and ZCS turn-ON at the rated condition. Otherwise, the switch conducts reversely during a particular interval at the beginning of each ON-state period. The switch current i_S normalized by the rated input current $I_{\text{dc\_}r}$ is given by

$$i_{Sn}(\omega t) = \frac{i_S(\omega t)}{I_{\text{dc\_}r}} = \begin{cases} \frac{2p_e}{p_{e\_r}\cdot G_v}\cdot \sin(\omega t+\pi) + i_{Lfn}(\omega t) & 0 < \omega t \le \pi \\ 0 & \pi < \omega t \le 2\pi. \end{cases} \tag{34}$$

III. *LCC-S* Resonant Class E^2 Topology for MHz-WPT Applications

This section proposes a push–pull Class E^2 topology as in Fig. 5 for MHz-WPT applications. The active Class E rectifier is implemented and has ZPA input irrelevant to load resistance. Besides, the *LCC-S* resonant tank realizes impedance conversion with zero phase shift. Eventually, the push–pull Class E^2 topology features load-independent ZVS operation and constant voltage gain.

A. Active Class E Rectifier With Coupled Inductor

As analyzed in Section II, the conventional inductor-coupled push–pull Class E topology has variable ZVS phases. Thus, it requires complex switching control when implemented as active rectification. Moreover, the rectifier's input phase varies with load resistance and causes complicated effects on the switching behavior of the inverter on the transmitter [27]. On the other hand, the proposed load-independent topology has an invariable ZVS phase. Thus, the switching phase control can be simplified significantly for achieving soft-switching.

According to the time-domain modeling and Fourier series in Section II, the rectifier's input impedance R_{rec} is given by

$$R_{\text{rec}} = 0.5\pi^2 R_L \tag{35}$$

where R_{rec} maintains ZPA regardless of the load resistance R_L variation. The parameters for the active rectifiers are identical to that of the inverters.

As in Fig. 6, the synchronous switches maintain the ZVS turn-ON over the entire load range, including $R_L < R_{\text{dc\_}r}$. Thus, it is worth noting that the active rectifiers perform better soft-switching behavior than the inverters. Besides, the ZCS turn-OFF is realized at $R_L = R_{\text{dc\_}r}$. Similar to the inverters, the reverse voltage occurs during an interval at the beginning of each OFF-state period when $R_L < R_{\text{dc\_}r}$. As in Fig. 7, the switches carry forward currents during an interval of each ON-state period. Thus, the load-independent rectification cannot be handled by diode-based rectifiers. Fig. 8 illustrates the currents through the output inductor L_{out}. It also features low-harmonic contents and large current amplitude at various loads.

B. LCC-S Resonant Tank

The *LCC-S* resonant tank can realize constant voltage gain and impedance conversion without phase shift. Thus, the inverter's load maintains resistive since the active rectifier has load-independent ZPA input. Thus, both the inverter and the active rectifier can maintain load-independent operation when connected through the *LCC-S* tank, of which parameters satisfy

$$\frac{1}{\omega^2} = L_1C_1 = L_2C_{2\text{eq}} = L_3C_3 \tag{36}$$

where $C_{2\text{eq}} = C_1C_2/(C_1+C_2)$, and thus, it comprises three resonant loops, which realizes a voltage gain expressed as

$$G_r = \frac{k_{23}\sqrt{L_2L_3}}{L_1} \tag{37}$$

where k_{23} is the coupling coefficient between the transmitting coil and the receiving coil. As the push–pull Class E^2 topology is symmetric, the dc–dc voltage gain of the system is identical to the *LCC-S* tank, i.e., $G_{\text{sys}} = G_r$. This equation is still valid when $G_r \neq 1$ since both the inverter and the rectifier have constant voltage gains.

The proposed push–pull Class E^2 topology has a load-independent voltage gain, proportional to the coupling coefficient between the transmitting coil and the receiving coil.

C. Magnetic Structure of Coupled Inductors With Enhanced Self-Inductance

As analyzed above, the coupled inductors dominate the suppression of current ripples on dc sides. The equivalent self-inductance can be increased with winding turns or magnetic core volumes. However, the overall losses will substantially increase due to the large amplitudes of harmonic currents. Therefore, the

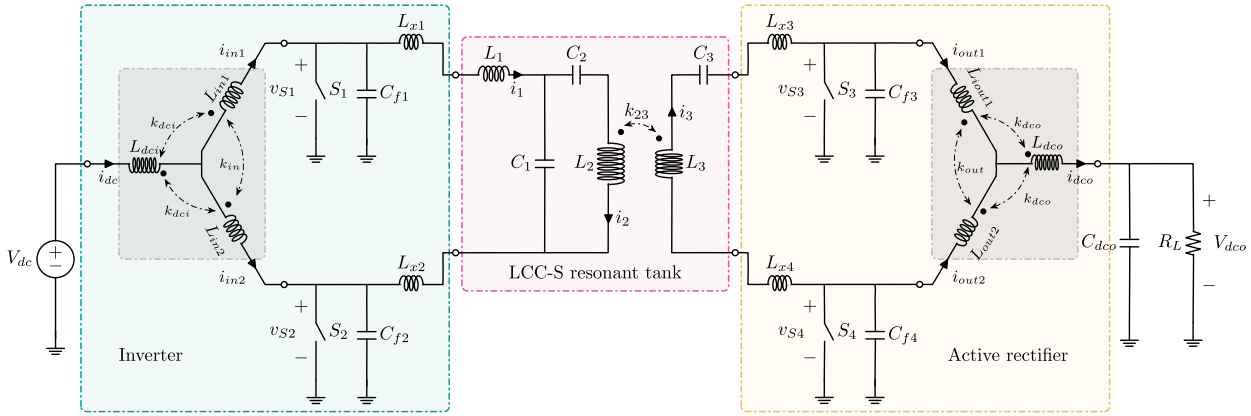

Fig. 5. Proposed push–pull Class E^2 topology with the three-winding magnetic structure for MHz-WPT applications. The additional inductance L_x can be merged with L_1 and L_3, respectively.

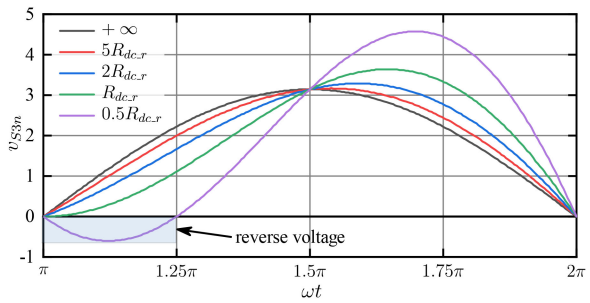

Fig. 6. Switch voltage v_{S3} of the active rectifier normalized by v_{dco}. The switches maintain soft-switching as R_L varies. Note that $v_{S3}(\omega t) = v_{S4}(\omega t + \pi)$.

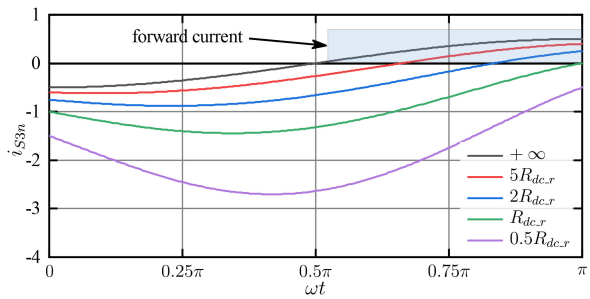

Fig. 7. Switch current i_{S3} of the active rectifier normalized by the rated I_{dco}. The forward current cannot be handled by diode-based rectifier.

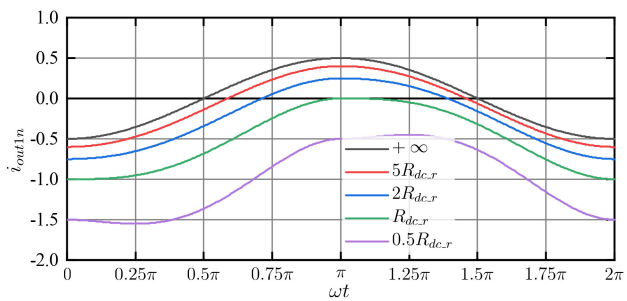

Fig. 8. Inductor current i_{out1} normalized by the rated I_{dco}. The current amplitude is nearly constant as R_{dc} varies.

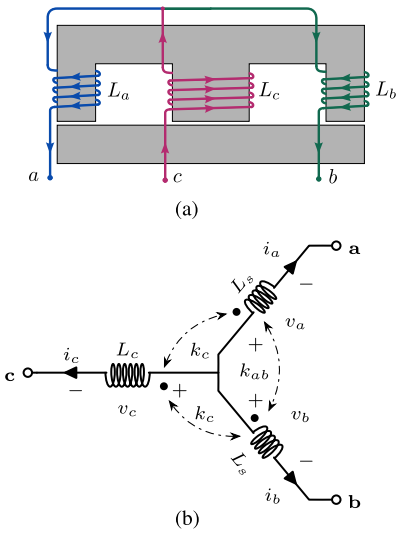

Fig. 9. (a) Proposed three-winding magnetic structure. (b) Equivalent circuit. Both the coupling coefficients are negative, i.e., $k_{ab}, k_c < 0$.

conventional magnetic structures of two windings are difficult to implement sufficient self-inductance [27], [28].

As in Fig. 9, a three-winding magnetic structure is proposed to improve the coupled inductors. With the additional winding, the equivalent self-inductance can be increased individually without increasing the turns carrying large harmonic currents. As illustrated in Fig. 9(b), since the structure is symmetrical, $L_a = L_b = L_s$. The equivalent circuit gives

$$\begin{bmatrix} v_a \\ v_b \\ v_c \end{bmatrix} = \begin{bmatrix} L_s & k_{ab}L_s & k_c\sqrt{L_sL_c} \\ k_{ab}L_s & L_s & k_c\sqrt{L_sL_c} \\ k_c\sqrt{L_sL_c} & k_c\sqrt{L_sL_c} & L_c \end{bmatrix} \begin{bmatrix} \frac{di_a}{dt} \\ \frac{di_b}{dt} \\ \frac{di_c}{dt} \end{bmatrix}. \quad (38)$$

Rearranging the equations gives

$$\begin{bmatrix} v_{\mathbf{ca}} \\ v_{\mathbf{cb}} \end{bmatrix} = \begin{bmatrix} L_m + L_f & L_m \\ L_m & L_m + L_f \end{bmatrix} \begin{bmatrix} \frac{di_a}{dt} \\ \frac{di_b}{dt} \end{bmatrix} \quad (39)$$

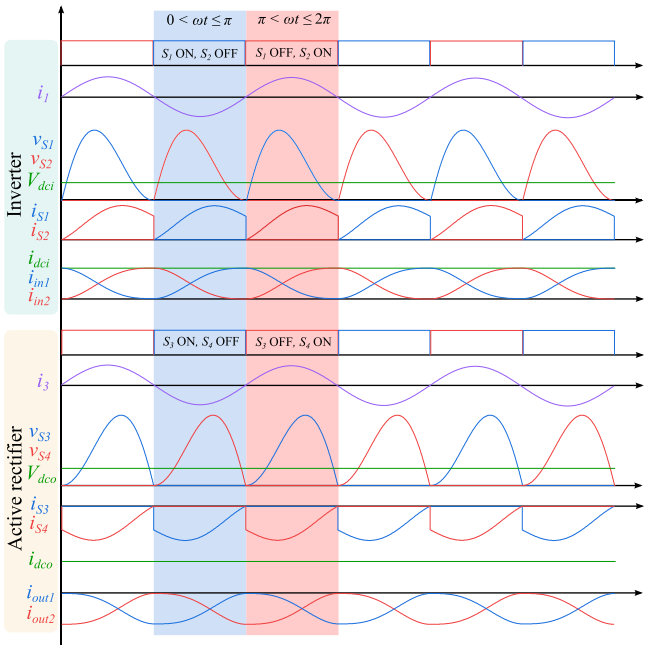

Fig. 10. Theoretical waveforms of the proposed *LCC-S* resonant Class E^2 topology for MHz-WPT applications. It features low-harmonic contents and ideal soft switching. The theoretical input and output currents have zero ripples.

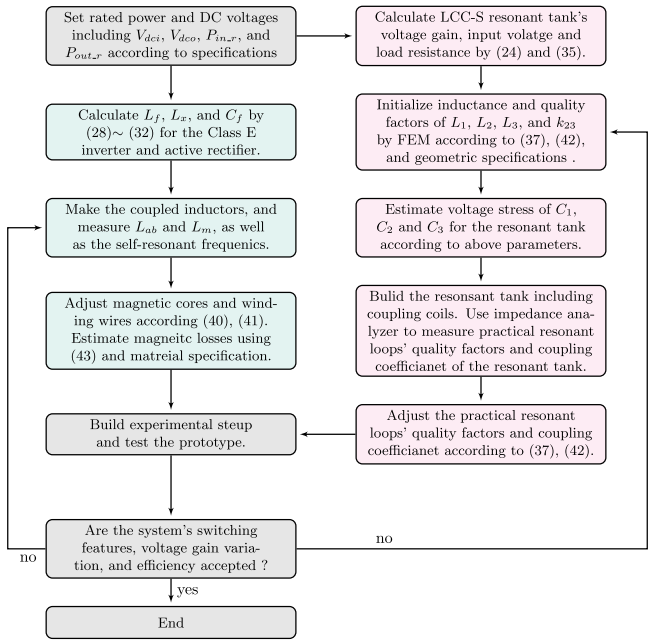

Fig. 11. Process of designing a practical MHz-WPT system based on the proposed load-independent Class E^2 converter with coupled inductors.

where L_m and L_f are the equivalent decoupled inductance in Fig. 1(b) given by

$$L_m = L_c + k_{ab}L_s - 2k_c\sqrt{L_sL_c} \tag{40}$$

$$L_f = (1-k_{ab})L_s = \frac{L_{\mathbf{ab}}}{2} \tag{41}$$

where $L_{\mathbf{ab}}$ is the inductance between terminals **a** and **b**. Thus, the equivalent self-inductance can be enhanced by increased L_c without increasing the turns of L_a and L_b. Meanwhile, L_f depends only on the coupled L_a and L_b, and is irreverent to L_c. Eventually, the proposed magnetic structure provides a simplified method to implement the coupled inductors and obtain sufficient self-inductance for dramatically suppressing the harmonic currents on dc sides.

D. Theoretical Waveforms and Design Consideration

Fig. 10 illustrates the theoretical waveforms of the proposed Class E^2 converter at the rated operation condition. The peak switch voltage will decrease as R_L increases. Thus, it reaches the maximum peak value of about 3.6 $V_{\rm dc}$ at the rated load. Consequently, the processable power of the push–pull Class E^2 topology is limited by the relatively high-voltage stress of the switches.

For practical applications, the expected voltage gain of the *LCC-S* network depends on specifications, which may also include limitations of size, weight, etc. According to (37), various combinations of the parameters are available to realize an identical voltage gain and will lead to different efficiency. To improve the efficiency, the loaded quality factor can be appropriately adjusted according to the approximate constraint given by

$$Q_L = \frac{\omega L_3}{R_{\rm ac}} \approx \frac{1}{k_{23}\sqrt{\frac{Q_2}{Q_3} + G_r k_{23}\frac{Q_2}{Q_1}\sqrt{\frac{L_2}{L_3}}}} \tag{42}$$

which is simplified by assuming the quality factors of the resonant loops are much larger than $\frac{1}{k_{23}}$. This equation provides a concise way to arrange the coupling coils, of which parameters depend on the sizes and the numbers of turns.

As analyzed above, both $i_{\rm in}$ and $i_{\rm out}$ have fixed current amplitudes of about 0.5 I_{dc}. Thus, the magnetic core losses are dominated by the side columns. According to (30), the amplitude of magnetic flux density passing the side columns can be estimated by

$$B_m \approx \frac{1+k_{ab}}{1-k_{ab}} \cdot \frac{V_{\rm dc}}{4fN_fA_e} \tag{43}$$

where f is the operation frequency, and A_e is the effective cross-sectional area of the side columns, as illustrated in Fig. 9(a). The acceptable B_m depends on the loss characteristics of the magnetic cores, of which manufactures usually provide loss density curves versus B_m. Then, the number of turns for L_f can be properly selected according to (41) and (43).

As shown in Fig. 5, a practical MHz-WPT system comprises the inverter, active rectifier, and *LCC-S* resonant tank. To summarize the utilization of the above equations, a brief design process is illustrated in Fig. 11, which integrates the modeling presented before.

IV. Example Design and Implementation

This section is to verify the proposed methodology. A 6.78-MHz prototype is designed and implemented to realize unity voltage-conversion ratio by using the topology in Fig. 5.

TABLE I
PARAMETERS OF INVERTER AND ACTIVE RECTIFIER

L_{ab}	1.133 μH
L_x	142 nH
C_f	486 pF
Operation frequency	6.78 MHz
GaN FET ($S_{1\sim4}$)	GS66508T

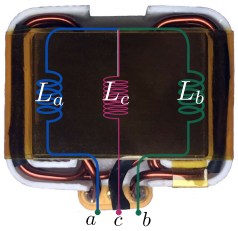

Fig. 12. Coupled inductor using EEQ25/11 magnetic core of Fair-Rite 67 material. A 3-D-printed skeleton is applied to fabricate the three windings.

A. Inverter and Active Rectifier

According to the design process illustrated in Fig. 11, the prototype's parameters in Table I are calculated by (29)–(32) and (41) with expected rated power and dc voltages. The inductance values have a straightforward rule as $L_f = 0.5L_{ab} = 4L_x$, which simplifies the design of the coupled inductors and the additional inductor.

For simplifying the design and comparison, the inverter and the rectifier have the same rated power and dc voltages, i.e., $P_{\text{in\_}r} = P_{\text{out\_}r} = 300$ W, $V_{\text{dci}} = V_{\text{dco}} = 48$ V in this design example. As analyzed above, the load-independent operation is conducive to preventing reverse conducting of GaN FETs at OFF-state. The switches are expected to achieve ZVS turn-ON over the designed load range.

As in Fig. 12, L_{in} and L_{out} are implemented by the same magnetic structure illustrated in Fig. 9. Considering i_c are dominated by direct current, the winding of L_c is made by solid copper wires of 0.6 mm diameter. In addition, since Litz wires are no longer effective for reducing winding losses at 6.78 MHz, solid wires of 1.2 mm diameter are applied for L_a and L_b, of which current amplitude is nearly constant at various loads. The measured L_{ab} is approximately 1 μH, and the self-inductance (i.e., L_{ac}, L_{bc}) is about 5 μH, which provides enough reactance to suppress the high-frequency current ripples.

A phase detector is implemented to detect and synchronize the driving phases of the synchronous switches. Since the input impedance of the active rectifier maintains ZPA regardless of load variation, the induced voltage of the receiving coil has a constant phase shift from the expected driving pulses. In this example, an auxiliary coil is applied to sense the induced voltage phase of the receiving coil [19]. As in Fig. 13, the auxiliary coil comprises three turns wound in different directions. By adjusting the pitches, the auxiliary coil is decoupled with the receiving coil but maintains a small mutual inductance with the transmitting coil. Then, the auxiliary coil can detect the induced voltage phase of the receiving coil, and avoid interference from the power stage. Two stages of monostable multivibrators are implemented to adjust the driving pulses' delay and duty cycles. As a result, the synchronous switches can be driven appropriately using the auxiliary coil and signal conditioning circuit.

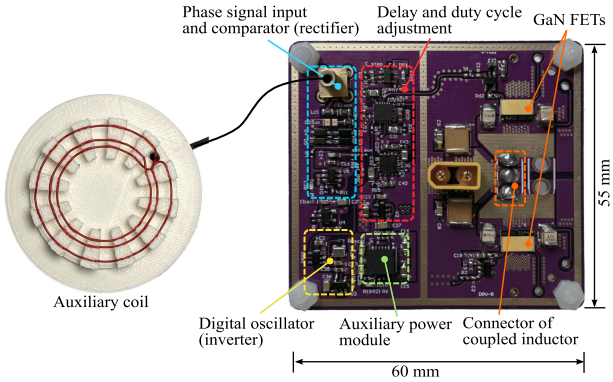

Fig. 13. Printed circuit board for the inverter and the active rectifier. The auxiliary coil provides an initial signal of phase reference for the synchronous switches of the rectifier. For the inverter, the driving pulses are generated by the digital oscillator on the PCB.

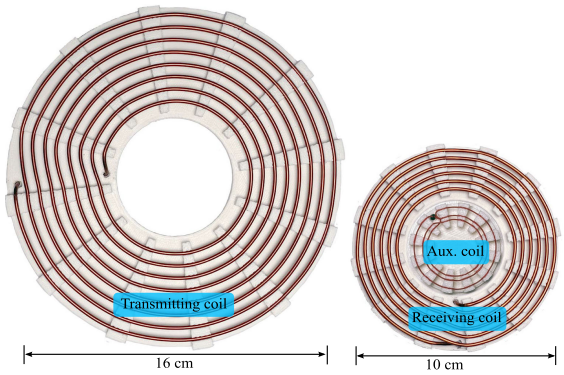

Fig. 14. Coupling coils. The auxiliary coil is fixed on the receiving coil. It is decoupled with the receiving coil but maintains a small mutual inductance with the transmitting coil.

The printed circuit board (PCB) in Fig. 13 is also implemented for the inverter. As phase synchronization is not necessary for inversion, a digital oscillator on PCB is applied to generate the driving pulses directly. Besides, a dc–dc module (TPSM5601) is used to power the gate drivers (1EDN7512) and the signal conditioning circuit.

B. LCC-S Compensated Coupling Coils

The geometry of coupling coils depends on particular applications. Generally, increasing coil size will result in lower self-resonant frequency (SRF). To compensate the coils properly and ensure the expected operation of the resonant tank, the SRF of the coupling coils should be much higher than 6.78 MHz. As in Fig. 14, the coupling coils are made by solid copper wires. The outer diameters of the transmitting coil and the receiving coil are 16 and 10 cm, respectively, and the pitches were adjusted according to full-wave finite element method (FEM) simulation. Eventually, the measured SRFs of the coupling coils are higher than 30 MHz, which satisfies the requirement of this example.

Table II illustrates the measured parameters of the resonant tank. The quality factors of L_1, L_2, and L_3 are 300, 371, and 446 at 6.78 MHz, respectively. To realize 1:1 voltage gain,

TABLE II
PARAMETERS OF *LCC-S* RESONANT TANK

Transmitting coil	Outer diameter	16 cm
	Number of turns	8
	Pitch	6 mm
	Wire diameter	1.8 mm
	Inductance L_2	10.33 μH
Receiving coil	Outer diameter	10 cm
	Number of turns	6
	Pitch	4 mm
	Wire diameter	1.7 mm
	Inductance L_3	3.94 μH
Compensation network	L_1	1.82 μH
	C_1	303.3 pF
	C_2	62.8 pF
	C_3	139.9 pF

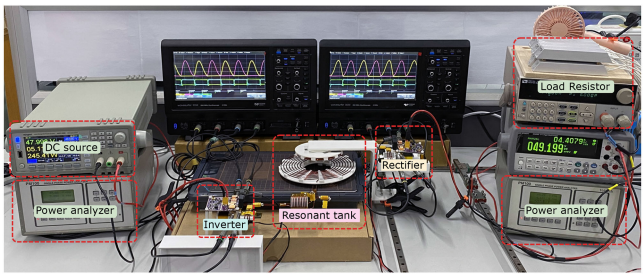

Fig. 15. Schematic diagram of the experimental setup.

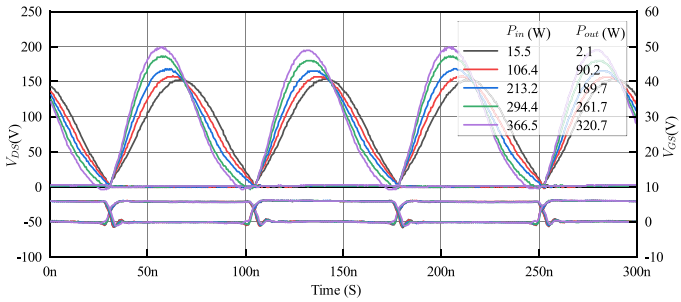

Fig. 16. Measured $V_{\rm ds}$ and $V_{\rm gs}$ of the inverter. The ZVS is maintained over the designed load range, i.e., $P_{\rm in} \leq 300$ W.

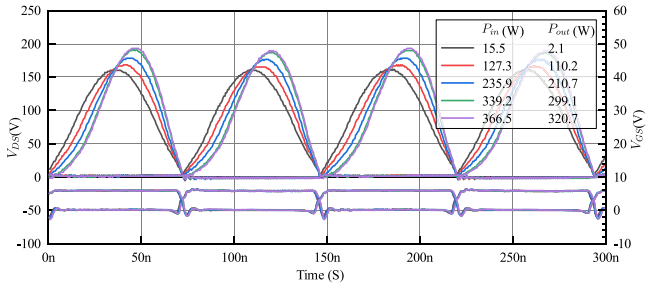

Fig. 17. Measured $V_{\rm ds}$ and $V_{\rm gs}$ of the active rectifier. The ZVS is maintained over the entire load range, including $P_{\rm out} > 300$ W.

the expected coupling coefficient meets $k_{23} = \frac{L_1}{\sqrt{L_2 \cdot L_3}} = 0.286$, corresponding to a transfer distance of about 2.5 cm. Thus, according to (42), the peak efficiency of the resonant tank is up to 97.8% at $Q_L = 2.952$, at which the output power is 200 W.

V. EXPERIMENTAL MEASUREMENT AND ANALYSIS

Fig. 15 shows the experimental setup of which the prototype comprises the inverter, the *LCC-S* resonant tank, and the active rectifier. The coupled inductors are connected under the PCBs. To limit the temperature rise of the switches and the inductors, single-layer copper foils are implemented as heat sinks of the GaN FETs with air cooling fans.

As the receiver has no external power source, the rectifier operates at passive rectification mode for milliseconds until the auxiliary power module is settled. The reverse-conducting threshold of the GaN FETs is about 2 V at $V_{\rm gs} = 0$. Thus, long-time passive rectification will degrade efficiency substantially due to the relatively high voltage drop of switches.

All the following measurements are obtained without adjusting circuit components. The relative position of the coupling coils is fixed with a measured $k_{23} = 0.29$. The operation frequency and the duty cycle are set at 6.78 MHz and 50%, respectively. Besides, the output voltage is fixed to 48 V by slightly adjusting the input voltage.

Fig. 16 illustrates the measured $V_{\rm ds}$ and $V_{\rm gs}$ of the inverter at various loads. The switches maintain ZVS turn-ON when the input power $P_{\rm in}$ is below 300 W, and the peak $V_{\rm ds}$ increases with the power level. The $V_{\rm ds}$ curves cross at $\omega \approx 1.5\pi$ during the OFF interval of each period. When $P_{\rm in} = 294.4$ W, the voltage derivative of $V_{\rm ds}$ at turn-ON instant is near zero. Thus, the switches achieve both ZVS and ZCS turn-ON when $P_{\rm in}$ is close to the rated input power. Otherwise, when the input power exceeds 300 W, the switches will conduct reversely during a short interval before the rising edge of each turn-ON pulse. Therefore, the measured $V_{\rm ds}$ matches well with the calculated curves illustrated in Fig. 2.

As illustrated in Fig. 17, the active rectifier acts as a time-reversal inverter. The measured $V_{\rm ds}$ curves also cross at $\omega \approx 1.5\pi$, and show a nearly mirrored image of the inverter. The switches maintain ZVS turn-ON over the entire load range, including $P_{\rm out} > 300$ W. At $P_{\rm out} = 320.7$ W as the output power exceeds the rated value, $V_{\rm ds}$ does not rise immediately, which means the synchronous switches conduct reversely during a short interval after the rising edge of each turn-OFF pulse. However, the OFF-state switches can commutate naturally and realize ZCS turn-OFF. Thus, the active rectifier performs better soft switching behavior than the inverter. Comparing the measured $V_{\rm ds}$ to that calculated in Fig. 6, the rectifier shows consistent switching behavior with the analysis before.

Fig. 18(a) shows measured $i_{\rm in1}$ and $i_{\rm out1}$ by a current probe of 120 MHz bandwidth. According to the modeling before, the theoretical i_{Lf} maintains an amplitude of $0.5I_{\rm dc\_r}$, where $I_{\rm dc\_r} = 6.25$ A for this design example. The measured currents are approximately sinusoidal, which match well with the calculated ones. It can be seen that the measured current amplitudes are slightly higher than the theoretical values illustrated in Figs. 3 and 8. In order to compare the measured currents with the analytical modeling, Fig. 18(b) illustrates the corresponding fast-Fourier transform (FFT) results. The fundamental current amplitudes maintain about 3.6 A at various loads. Besides, the dc offset increases with power level, and reaches about 3.2 A at the

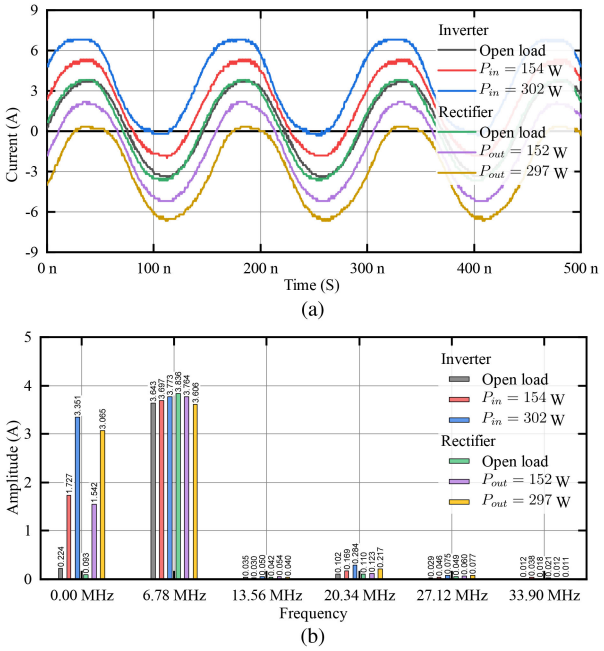

Fig. 18. (a) Measured i_{in1} and i_{out1}. (b) FFT results. The push–pull Class E^2 topology features low-harmonic contents.

rated input/output power of 300 W. Considering the measured L_{ab} of about 1 μH is slightly lower than the calculated inductance of 1.133 μH in Table I, the winding currents performed expected features as analysis before. The spectrum is dominated by dc and fundamental frequency at 6.78 MHz of which amplitudes are nearly constant at various loads. The even-order harmonics are well suppressed as the amplitudes are negligible at 13.56 and 27.12 MHz. The three-winding magnetic structure performs better suppression performance than that in [27]. As in Fig. 9, the fundamental current circulates between L_a and L_b, and thus the measured harmonic distribution implies that the ripples of i_{dci} and i_{dco} are negligible. It validates that the proposed magnetic structure is conducive to suppressing current noises on the dc sides and performs better filtering features than the conventional push–pull Class E topology with coupled inductors.

Fig. 19 shows the steady-state thermal images. The overall temperature rise increases with processed power and is dominated by the switches and the coupled inductors. The temperature rise of the GaN FETs shows slightly unbalanced due to the relatively high temperature of the auxiliary power module TPSM5601. According to the circuit modeling above, the fundamental current has to maintain a relatively high amplitude to realize load-independent ZVS operation. Consequently, the Class E^2 converter has relatively high no-load losses, which will reduce the efficiency at light-load conditions.

Fig. 20 shows the efficiencies and the voltage gain of the prototype. The output dc voltage is fixed at 48 V by slightly adjusting the input power supply. The maximum system efficiency is 89.3% at 210-W output power, and it will reach 90.4% when excluding the driving losses of which the measured value is 1.42 W for each side. Since the inverter and the active rectifier use the same parameters and present nearly symmetrical waveforms,

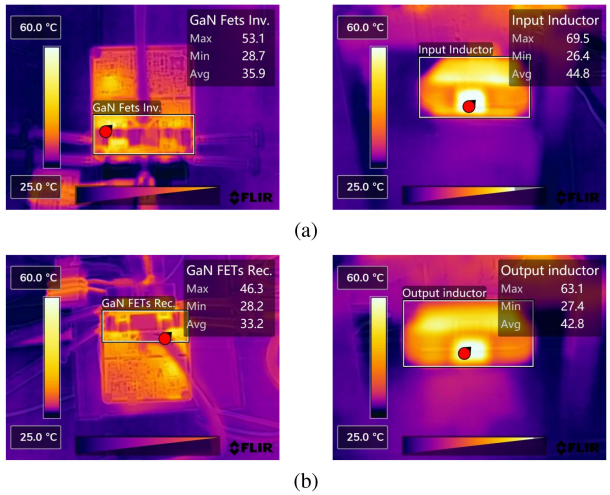

Fig. 19. Thermal images of the prototype with 339 W input to 300 W output. (a) Inverter. (b) Active rectifier. The total losses are dominated by the switches and the coupled inductors.

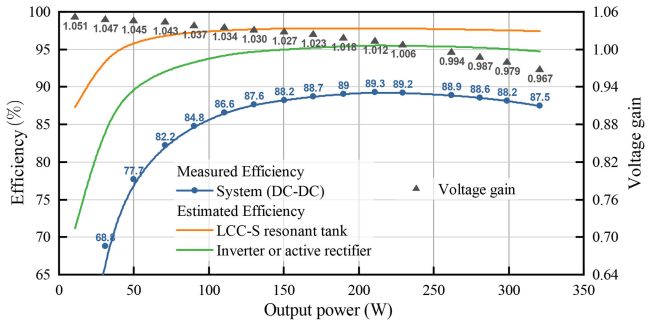

Fig. 20. Efficiencies and voltage gain.

it is reasonable to assume that they have approximately equal efficiencies. Therefore, the efficiencies of the *LCC-S* resonant tank, the inverter, and the rectifier are also estimated in the figure. The maximum efficiency of the inverter (or the active rectifier) reaches 95.6%.

As modeling in Section II, the load-independent operation achieves constant voltage gain for both the inverter and active rectifier. Considering the power losses of practical systems, the measured voltage gain will decrease with output power. As illustrated in the figure, the measured voltage gain, i.e., $V_{\text{dco}}/V_{\text{dci}}$, decreases slowly with the output power. It varies between +5/−4% over the entire load range. Hence, the prototype presents the expected load-independent operation of the push–pull Class E^2 topology with coupled inductors.

VI. Conclusion

This article models and implements the inductor-coupled push–pull Class E topology achieving the load-independent operation, which performs distantly improved soft-switching performance, load regulation, harmonics suppression, and efficiency compared with the previous work [27]. A prototype is built and the proposed methodology is verified. The following conclusions can be made.

1) The modeling validates that the inductor-coupled Class E topology is able to achieve the load-independent operation, which performs strict ZVS and constant voltage gain regardless of load variation. The measured switch voltages match well with the theoretical calculated.
2) The active rectifier performs better soft-switching than the inverter. The analysis and measurement show that the rectifier achieves load-independent ZVS even when the output power excesses the rated value.
3) The proposed three-winding magnetic structure realizes much higher equivalent self-inductance, which dominates the suppression of harmonic currents. The measured FFT results indicate that the prototype features negligible current ripples on dc sides.
4) The proposed *LCC-S* resonant Class E^2 converter features negligible harmonic contents and maintains soft switching with a constant voltage conversion ratio over the entire load range. The prototype realizes load-independent ZVS and maintains an approximately constant voltage gain with $+5/-4\%$ variance from no-load to 320-W output power. The measured dc–dc efficiency reaches 89.3% at 210 W.

REFERENCES

[1] Z. Zhang, H. Pang, A. Georgiadis, and C. Cecati, "Wireless power transfer-An overview," *IEEE Trans. Ind. Electron.*, vol. 66, no. 2, pp. 1044–1058, Feb. 2019.

[2] J. Feng, Q. Li, F. C. Lee, and M. Fu, "LCCL-LC resonant converter and its soft switching realization for omnidirectional wireless power transfer systems," *IEEE Trans. Power Electron.*, vol. 36, no. 4, pp. 3828–3839, Apr. 2021.

[3] M. J. Karimi, A. Schmid, and C. Dehollain, "Wireless power and data transmission for implanted devices via inductive links: A systematic review," *IEEE Sensors J.*, vol. 21, no. 6, pp. 7145–7161, Mar. 2021.

[4] C. R. Teeneti, T. T. Truscott, D. N. Beal, and Z. Pantic, "Review of wireless charging systems for autonomous underwater vehicles," *IEEE J. Ocean. Eng.*, vol. 46, no. 1, pp. 68–87, Jan. 2021.

[5] Y. Yao *et al.*, "Design and optimization of an electric vehicle wireless charging system using interleaved boost converter and flat solenoid coupler," *IEEE Trans. Power Electron.*, vol. 36, no. 4, pp. 3894–3908, Apr. 2021.

[6] H. Tebianian, Y. Salami, B. Jeyasurya, and J. E. Quaicoe, "A 13.56-MHz full-bridge class-D ZVS inverter with dynamic dead-time control for wireless power transfer systems," *IEEE Trans. Ind. Electron.*, vol. 67, no. 2, pp. 1487–1497, Feb. 2020.

[7] L. Gu, G. Zulauf, A. Stein, P. A. Kyaw, T. Chen, and J. M. R. Davila, "6.78-MHz wireless power transfer with self-resonant coils at 95% DC–DC efficiency," *IEEE Trans. Power Electron.*, vol. 36, no. 3, pp. 2456–2460, Mar. 2021.

[8] H. Oh *et al.*, "6.78 MHz wireless power transmitter based on a reconfigurable class-E power amplifier for multiple device charging," *IEEE Trans. Power Electron.*, vol. 35, no. 6, pp. 5907–5917, Jun. 2020.

[9] A. Ayachit, F. Corti, A. Reatti, and M. K. Kazimierczuk, "Zero-voltage switching operation of transformer class-E inverter at any coupling coefficient," *IEEE Trans. Ind. Electron.*, vol. 66, no. 3, pp. 1809–1819, Mar. 2019.

[10] M. Fu, H. Yin, M. Liu, Y. Wang, and C. Ma, "A 6.78 MHz multiple-receiver wireless power transfer system with constant output voltage and optimum efficiency," *IEEE Trans. Power Electron.*, vol. 33, no. 6, pp. 5330–5340, Jun. 2018.

[11] M. Liu, Y. Qiao, S. Liu, and C. Ma, "Analysis and design of a. robust class E^2 DC–DC converter for megahertz wireless power transfer," *IEEE Trans. Power Electron.*, vol. 32, no. 4, pp. 2835–2845, Apr. 2017.

[12] Y. Li, X. Ruan, L. Zhang, J. Dai, and Q. Jin, "Optimized parameters design and adaptive duty-cycle adjustment for class E DC–DC converter with on–off control," *IEEE Trans. Power Electron.*, vol. 34, no. 8, pp. 7728–7744, Aug. 2019.

[13] L. Roslaniec, A. S. Jurkov, A. A. Bastami, and D. J. Perreault, "Design of single-switch inverters for variable resistance/load modulation operation," *IEEE Trans. Power Electron.*, vol. 30, no. 6, pp. 3200–3214, Jun. 2015.

[14] S. Aldhaher, D. C. Yates, and P. D. Mitcheson, "Load-independent class E/EF inverters and rectifiers for MHz-switching applications," *IEEE Trans. Power Electron.*, vol. 33, no. 10, pp. 8270–8287, Oct. 2018.

[15] Z. Kaczmarczyk and W. Jurczak, "A push–pull class-E inverter with improved efficiency," *IEEE Trans. Ind. Electron.*, vol. 55, no. 4, pp. 1871–1874, Apr. 2008.

[16] H. Mousavian, S. Abnavi, A. Bakhshai, and P. Jain, "A push–pull class E converter with improved PDM control," in *Proc. IEEE 7th Int. Symp. Power Electron. Distrib. Gener. Syst.*, Vancouver, BC, Canada, 2016, pp. 1–6.

[17] Y. Dou, X. Huang, Z. Ouyang, and M. A. Andersen, "Modelling and compensation design of class-E rectifier for near-resistive impedance in high-frequency power conversion," *IEEE Trans. Power Electron.*, vol. 36, no. 8, pp. 8812–8823, Aug. 2021.

[18] M. Liu and M. Chen, "Dual-band wireless power transfer with reactance steering network and reconfigurable receivers," *IEEE Trans. Power Electron.*, vol. 35, no. 1, pp. 496–507, Jan. 2020.

[19] X. Huang, Y. Dou, S. Lin, Y. Tian, Z. Ouyang, and M. A. E. Andersen, "Synchronous push–pull class E rectifiers with load-independent operation for megahertz wireless power transfer," *IEEE Trans. Power Electron.*, vol. 36, no. 6, pp. 6351–6363, Jun. 2021.

[20] L. Gu, G. Zulauf, Z. Zhang, S. Chakraborty, and J. Rivas-Davila, "Push–pull class Φ_2 RF power amplifier," *IEEE Trans. Power Electron.*, vol. 35, no. 10, pp. 10515–10531, Oct. 2020.

[21] L. Gu and J. Rivas-Davila, "1.7 kW 6.78 MHz wireless power transfer with air-core coils at 95.7% DC–DC efficiency," in *Proc. IEEE Wireless Power Transf. Conf.*, San Diego, CA, USA, 2021, pp. 1–4.

[22] Z. Zhang *et al.*, "GaN VHF converters with integrated air-core transformers," *IEEE Trans. Power Electron.*, vol. 34, no. 4, pp. 3504–3515, Apr. 2019.

[23] D. K. Saini, A. Ayachit, A. Reatti, and M. K. Kazimierczuk, "Analysis and design of choke inductors for switched-mode power inverters," *IEEE Trans. Ind. Electron.*, vol. 65, no. 3, pp. 2234–2244, Mar. 2018.

[24] N. Pucci, J. M. Arteaga, C. Kwan, D. C. Yates, and P. D. Mitcheson, "Induced voltage estimation from class EF switching harmonics in HF-IPT systems," *IEEE Trans. Power Electron.*, vol. 37, no. 4, pp. 4903–4916, Apr. 2022.

[25] K. Surakitbovorn and J. Rivas-Davilla, "Design of a GaN-based wireless power transfer system at 13.56 MHz to replace conventional wired connection in a vehicle," in *Proc. Int. Power Electron. Conf.*, 2018, pp. 3848–3854.

[26] A. J. Hanson, J. A. Belk, S. Lim, C. R. Sullivan, and D. J. Perreault, "Measurements and performance factor comparisons of magnetic materials at high frequency," *IEEE Trans. Power Electron.*, vol. 31, no. 11, pp. 7909–7925, Nov. 2016.

[27] X. Huang, Y. Kong, Z. Ouyang, W. Chen, and S. Lin, "Analysis and comparison of push–pull class-E inverters with magnetic integration for megahertz wireless power transfer," *IEEE Trans. Power Electron.*, vol. 35, no. 1, pp. 565–577, Jan. 2020.

[28] K. Li, S. C. Tan, and R. S. Y. Hui, "Single-stage regulated resonant WPT receiver with low input harmonic distortion," *IEEE Trans. Power Electron.*, vol. 35, no. 7, pp. 6820–6829, Jul. 2020.

[29] R. E. Zulinski and K. J. Grady, "Load-independent class E power inverters—Part I: Theoretical development," *IEEE Trans. Circuits Syst.*, vol. 37, no. 8, pp. 1010–1018, Aug. 1990.

Xiaosheng Huang (Member, IEEE) received the B.E. and Ph.D. degrees from Fuzhou University, Fuzhou, China, in 2009 and 2015, respectively.

He is currently an Associate Professor with the School of Electronic, Electrical Engineering and Physics, Fujian University of Technology, Fuzhou, China, and also with the Fujian Provincial University Engineering Research Center for Industrial Automation, Fujian University of Technology. His research interests include power conversion, high-frequency magnetics, wireless power transfer, and electromagnetic field analysis and applications.

Dr. Huang is a member of the Magnetic Component Specialty Committee of the China Power Supply Society.

Zhikun Yu received the B.E. degree from Putian University, Fujian, China, in 2018. He is currently working toward the M.E. degree with the School of Electronic, Electrical Engineering and Physics, Fujian University of Technology, Fuzhou, China.

His research interests include wireless power transfer and optimization of high-frequency magnetics.

Yi Dou (Member, IEEE) received the M.Sc. and Ph.D. degrees in power electronics from the Technical University of Denmark, Kongens Lyngby, Denmark, in 2018 and 2022, respectively.

He is currently a Senior Power Electronics Engineer with Resonant Link, Shelburne, VT, USA, focusing on research and development in wireless power transfer systems for implanted medical devices. His research interests include design of high-frequency dc–dc converters, modeling and design for magnetic components, and modeling and optimization of MHz-range wireless power transfer systems.

Shuyi Lin received the B.E. and Ph.D. degrees from Fuzhou University, Fuzhou, China, in 2008 and 2014, respectively.

She is currently an Associate Professor with the School of Electronic, Electrical Engineering and Physics, Fujian University of Technology, Fuzhou, China, and also with the Fujian Provincial University Engineering Research Center for Industrial Automation, Fujian University of Technology. Her research interests include power conversion, high-frequency magnetics, and wireless power transfer.

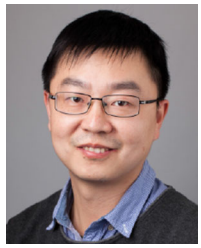

Ziwei Ouyang (Senior Member, IEEE) received the Ph.D. degree from the Technical University of Denmark (DTU), Kongens Lyngby, Denmark, in 2011.

From 2011 to 2013, he was a Postdoctoral Researcher with DTU. Since 2013, he has been an Assistant Professor with DTU, where he has been an Associate Professor since 2016. His research interests include high-frequency planar magnetics modeling and integration, high-density high-efficiency power converters, PV battery energy storage system, and wireless charging. He has authored or co-authored more than 70 high-impact IEEE journal and conference publications, and has co-authored a book chapter on Magnetics for the "Handbook of Power Electronics" and he is currently the holder of eight international patents.

Dr. Ouyang was a recipient of Young Engineer Award at PCIM Asia 2014, the Best Ph.D. Dissertation of the Year Award 2012 from DTU, and several Best Paper Awards in IEEE-sponsored international conferences. He has been invited to give lectures in many universities, enterprises, and educational seminars and workshops around the world, including the USA, Europe, and China. He was Session Chair in some IEEE-sponsored conferences and an Associate Editor for the *IEEE Journal of Emerging and Selected Topics in Power Electronics*.

Michael A. E. Andersen (Member, IEEE) received the M.Sc.E.E. and Ph.D. degrees in power electronics from the Technical University of Denmark, Kongens Lyngby, Denmark, in 1987 and 1990, respectively.

He is currently a Professor of power electronics with the Technical University of Denmark, where he has been the Deputy Head of the Department of Electrical Engineering, since 2009. He has authored or co-authored more than 300 publications. His research interests include switch-mode power supplies, piezoelectric transformers, power factor correction, and switch-mode audio power amplifiers.